

A 2D HYBRID MODEL FOR ULTRASONIC PULSE-ECHO SCATTERING FROM A ROUGH INTERFACE BURIED IN A LAYERED MEDIUM

Smaine Zeroug and Yong-Hua Chen

Schlumberger-Doll Research, Ridgefield, CT 06877

INTRODUCTION

Understanding and predicting the effects of surface roughness on ultrasonic pulse-echo measurements is important in a variety of applications. In particular, it is of interest for cased well evaluation in the oilfield industry where the measurement is used to investigate the cement seal placed between the casing and the formation wall (see Fig. 1(a)) [1]. Here, the acoustic transducer signal arises from multiple reflections taking place at the various interfaces of the layered (borehole fluid)-(steel casing)-cement-(rocky formation) structure. Previous numerical models, developed to account for this measurement, have been limited to canonical configurations where, in particular, the various interfaces are smooth [2]. Typically, the cement-formation interface is rough with widely varying rms height and correlation length. In order to predict the effect of roughness of *arbitrary size* on the reflection echo attributed to this interface, a frequency-domain hybrid analytical/numerical simulation model has been developed. The model has been preliminary implemented for a two-dimensional (2D) configuration where an acoustic transducer with a Gaussian profile interacts with the aforementioned structure in a planar geometry (see Fig. 1(b)). In this configuration, the transducer aperture has a finite size in the (x, z) and is infinite in the y direction. The fluid, steel layer, cement layer, and halfspace formation are assumed to be isotropic and homogeneous. The cement-formation interface, denoted by S_0 , is in general irregular or rough and parameterized by the function $z = h(x)$ describing the height of a particle on S_0 measured from the (mean) plane $z = 0$. A time-harmonic variation $e^{i\omega t}$ is assumed throughout.

The transducer voltage due to the entire configuration can be written as the sum of two separate contributions: the first arising from the configuration with S_0 removed to infinity and the second, $e_{\mathcal{R}}^{S_0}$, due to the presence of S_0 . Because of space limitation, we restrict the content of this paper to the calculation of $e_{\mathcal{R}}^{S_0}$ only. A more complete manuscript containing the calculation for the total voltage is prepared for submission elsewhere. In the formulation used, the transmitting/receiving transducer is modeled via the complex-transducer-point (CTP) technique [3] which simulates radiating and receiving transducers with Gaussian distributions. The interaction of the transducer beam with the fluid-steel-(infinite cement) configuration is treated analytically using spectral plane-wave integral representations. A real-axis integration scheme for the resulting integrals is used to compute the transmitted elastic wave fields in the cement. The scattering of the transmitted wave fields from the cement-formation rough interface is formulated via a surface integral equation which is solved numerically using the boundary element method (BEM). Finally, a surface integral is used to express the transducer voltage attributed to scattering from the

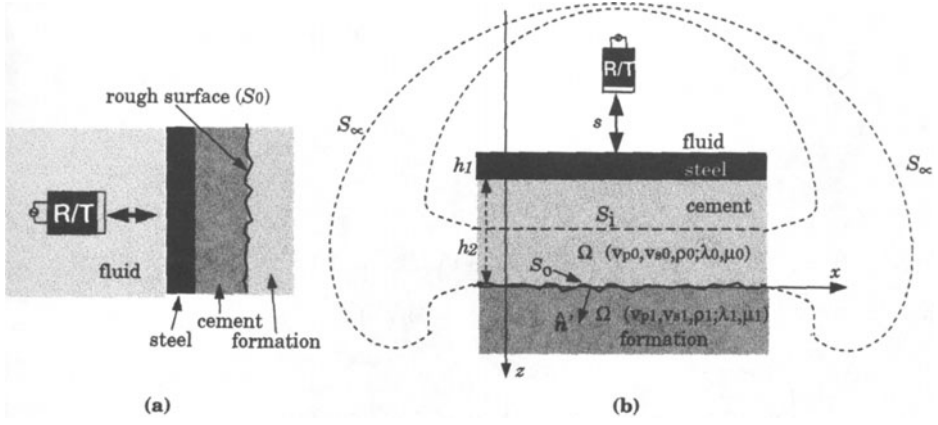


Figure 1. (a) Schematic of ultrasonic pulse-echo measurement in a cased well (only half of the vertical cut is shown). (b) Geometry of 2D configuration studied shown with a rough interface S_0 separating cement (Ω_0) from formation (Ω_1). The part surrounded by S_i is treated analytically to provide the incident wave fields on S_0 . It is assumed that the incident and scattered fields are negligible on the continuation S_∞ of S_0 . s : transducer-steel standoff, h_1 : steel layer thickness, h_2 : thickness of cement.

rough interface. In the following, we briefly describe the ingredients of this hybrid model and present illustrative numerical results.

THEORY

Voltage Formulation

Using formulae adapted from deHoop [4], $e_{\mathcal{R}}^{S_0}$ can be expressed as a line integral at S_0 (see Fig. 1(b)),

$$e_{\mathcal{R}}^{S_0} = i\omega\gamma(\omega) \int_{S_0} \left(\bar{\mathbf{T}}^{\text{sc}} \cdot \mathbf{u}^{\mathcal{R}} - \bar{\mathbf{T}}^{\mathcal{R}} \cdot \mathbf{u}^{\text{sc}} \right) \cdot \hat{\mathbf{n}}' dl', \quad (1)$$

where $(\bar{\mathbf{T}}^{\text{sc}}, \mathbf{u}^{\text{sc}})$ are the scattered stress tensor and particle displacement fields from S_0 and $(\bar{\mathbf{T}}^{\mathcal{R}}, \mathbf{u}^{\mathcal{R}})$ the corresponding quantities radiated by \mathcal{R} (when energized) via the steel layer and evaluated in the cement layer; $\hat{\mathbf{n}}'$ is the normal to S_0 whereas dl' is a curvilinear element of integration along S_0 . The quantity $\gamma(\omega)$ is added here to accommodate the transfer function of the transducer-electronics system. Solutions for $(\bar{\mathbf{T}}^{\text{sc}}, \mathbf{u}^{\text{sc}})$ require knowledge of the incident wave fields on S_0 . Let $(\bar{\mathbf{T}}^{\mathcal{T}}, \mathbf{u}^{\mathcal{T}})$ denote these incident quantities. We proceed next with the spectral integral formulations for evaluating $(\bar{\mathbf{T}}^{\mathcal{T}, \mathcal{R}}, \mathbf{u}^{\mathcal{T}, \mathcal{R}})$.

Transmitted Wave Fields in Cement Layer

The transmitted displacement fields due to \mathcal{T} ($\mathbf{u}^{\mathcal{T}}$) or to \mathcal{R} ($\mathbf{u}^{\mathcal{R}}$) can be derived from displacement potentials ($\phi^{\mathcal{T}, \mathcal{R}}$ and $\psi^{\mathcal{T}, \mathcal{R}}$) as follows,

$$\mathbf{u}^{\mathcal{T}, \mathcal{R}} = \nabla \phi^{\mathcal{T}, \mathcal{R}} + \nabla \times (\mathbf{0}, \psi^{\mathcal{T}, \mathcal{R}}, \mathbf{0}). \quad (2)$$

The corresponding stress fields are related to the displacement fields via the constitutive

relation,

$$\bar{\mathbf{T}}^{T,\mathcal{R}} = \lambda_0(\nabla \cdot \mathbf{u}^{T,\mathcal{R}})\bar{\mathbf{I}} + \mu_0[2\nabla\mathbf{u}^{T,\mathcal{R}} + \bar{\mathbf{I}} \times (\nabla \times \mathbf{u}^{T,\mathcal{R}})], \quad (3)$$

where $\bar{\mathbf{I}}$ is the identity tensor, and λ_0 and μ_0 are the Lamé constants of the cement (region Ω_0 in Fig. 1(b)). To solve for the relevant wave equations and boundary conditions at the various interfaces, we use spectral plane-wave representation of the form,

$$\{\phi^{T,\mathcal{R}}, \psi^{T,\mathcal{R}}\}(x, z) = \frac{1}{2\pi} \int_{-\infty}^{\infty} \{\hat{\phi}^{T,\mathcal{R}}, \hat{\psi}^{T,\mathcal{R}}\}(k; z) \exp\{ikx\} dk, \quad (4)$$

with $\hat{\phi}^{T,\mathcal{R}}(k; z)$ and $\hat{\psi}^{T,\mathcal{R}}(k; z)$ given by the inverse transform,

$$\{\hat{\phi}^{T,\mathcal{R}}, \hat{\psi}^{T,\mathcal{R}}\}(k; z) = \int_{-\infty}^{\infty} \{\phi^{T,\mathcal{R}}, \psi^{T,\mathcal{R}}\}(x, z) \exp\{-ikx\} dx. \quad (5)$$

Solutions for $\hat{\phi}^{T,\mathcal{R}}(k; z)$ and $\hat{\psi}^{T,\mathcal{R}}(k; z)$ can be written as,

$$\begin{Bmatrix} \hat{\phi}^{T,\mathcal{R}}(k; z) \\ \hat{\psi}^{T,\mathcal{R}}(k; z) \end{Bmatrix} = \frac{i}{2\kappa_f} \begin{Bmatrix} T_p^{\text{glob}}(k) \exp\{i\mathcal{P}_p(k)^{T,\mathcal{R}}\} \\ T_s^{\text{glob}}(k) \exp\{i\mathcal{P}_s(k)^{T,\mathcal{R}}\} \end{Bmatrix}, \quad (6)$$

with

$$\begin{Bmatrix} \mathcal{P}_p(k)^{T,\mathcal{R}} \\ \mathcal{P}_s(k)^{T,\mathcal{R}} \end{Bmatrix} = k(x - x_{T,\mathcal{R}}) - \kappa_f z_{T,\mathcal{R}} + \begin{Bmatrix} \kappa_{p0}(z - h_1) \\ \kappa_{s0}(z - h_1) \end{Bmatrix}, \quad h_1 < z < h_2, \quad (7)$$

and

$$\kappa_{f,p0,s0} = \sqrt{k_{f,p0,s0}^2 - k^2}, \quad \text{Im}\{\kappa_{f,p0,s0}\} > 0; \quad k_{f,p0,s0} = \omega/v_{f,p0,s0}. \quad (8)$$

In the above, T_p^{glob} and T_s^{glob} are P and S global plane-wave transmission coefficients that account for the fluid-steel-cement configuration, v_f is the sound speed in the fluid, v_{p0} and v_{s0} are the compressional and shear wave speeds in the cement, h_1 is the steel plate thickness, whereas $(x_{T,\mathcal{R}}, z_{T,\mathcal{R}})$ are the complex coordinates of the transmitting and receiving CTP; for pulse-echo mode $x_T = x_R$ and $z_T = z_R$. To solve for the pertinent components of $\mathbf{u}^{T,\mathcal{R}}$ and $\bar{\mathbf{T}}^{T,\mathcal{R}}$, we use similar spectral representation as in (4) and then carry out the various differentiation in (2) and (3) within the integral. For instance,

$$T_{zx}^{T,\mathcal{R}}(x, z) = \frac{1}{2\pi} \int_{-\infty}^{\infty} \hat{T}_{zx}^{T,\mathcal{R}}(k; z) \exp\{ikx\} dk, \quad (9)$$

$$\text{with} \quad \hat{T}_{zx}^{T,\mathcal{R}}(k; z) = \mu_0 \left\{ -2k\kappa_{p0}\hat{\phi}^{T,\mathcal{R}} - (k^2 - \kappa_{s0}^2)\hat{\psi}^{T,\mathcal{R}} \right\}. \quad (10)$$

Scattered Wave Fields from Rough Surface

We consider the interface S_0 separating Ω_0 and Ω_1 as shown in Fig. 1(b) with unit normal vector $\hat{n}' = \hat{n}(r') = (n_x \hat{x} + n_z \hat{z})$, insomified by the incident displacement field \mathbf{u}^T . Using the extinction theorem, volume integral equations can be established to yield the scattered wavefield \mathbf{u}^{sc} in Ω_0 and Ω_1 in terms of the traction and displacement wave fields on S_0 (as found in [5]). To solve for the latter unknowns we use the following surface integral equations which are obtained from the volume integral equations by letting the observation point approach S_0 and enforcing a well welded contact along S_0 (i.e., continuity of all displacement and stress components on S_0),

$$\frac{1}{2}\mathbf{u}(\mathbf{r}) + \oint_{S_0} \{\mathbf{u}(\mathbf{r}') \cdot [\hat{n}' \cdot \bar{\boldsymbol{\Sigma}}^0(\mathbf{r}, \mathbf{r}')] - [\hat{n}' \cdot \bar{\mathbf{T}}(\mathbf{r}')] \cdot \bar{\mathbf{G}}^0(\mathbf{r}, \mathbf{r}')\} d\ell' = \mathbf{u}^T(\mathbf{r}), \quad \mathbf{r} \in S_0, \quad (11)$$

$$-\frac{1}{2}\mathbf{u}(\mathbf{r}) + \oint_{S_0} \{\mathbf{u}(\mathbf{r}') \cdot [\hat{\mathbf{n}}' \cdot \bar{\bar{\Sigma}}^1(\mathbf{r}, \mathbf{r}')] - [\hat{\mathbf{n}}' \cdot \bar{\mathbf{T}}(\mathbf{r}')] \cdot \bar{\mathbf{G}}^1(\mathbf{r}, \mathbf{r}')\} d\mathbf{l}' = 0, \quad \mathbf{r} \in S_0, \quad (12)$$

where $\bar{\mathbf{G}}^{0,1}(\mathbf{r}, \mathbf{r}')$ and $\bar{\bar{\Sigma}}^{0,1}(\mathbf{r}, \mathbf{r}')$ are the unbounded-space Green's displacement tensor and the third rank Green's stress tensor in Ω_0 and Ω_1 . They can be expressed in terms of the unbounded-space compressional and shear 2D Green's function $g_{p,s} = i/4H_0^{(1)}(k_{p,s}|\mathbf{r} - \mathbf{r}'|)$ as shown in [5]. Letting

$$\begin{aligned} \hat{\mathbf{n}}' \cdot \bar{\mathbf{T}}(\mathbf{r}') &= (n_x T_{xx} + n_z T_{zx})\hat{\mathbf{x}} + (n_x T_{xz} + n_z T_{zz})\hat{\mathbf{z}} \\ &= T_x \hat{\mathbf{x}} + T_z \hat{\mathbf{z}}, \end{aligned} \quad (13)$$

and substituting the expression into the vector integral equations, we obtain four scalar integral equations. They are

$$\frac{1}{2}u_x + \oint_{S_0} \{u_x n_x \Sigma_{xxx}^0 + u_x n_z \Sigma_{xxz}^0 + u_z n_x \Sigma_{xzx}^0 + u_z n_z \Sigma_{zzx}^0 - T_x G_{xx}^0 - T_z G_{zx}^0\} d\mathbf{l}' = u_x^T(\mathbf{r}), \quad \mathbf{r} \in S_0, \quad (14)$$

$$\frac{1}{2}u_z + \oint_{S_0} \{u_z n_z \Sigma_{zzz}^0 + u_x n_x \Sigma_{xzz}^0 + u_x n_z \Sigma_{xxz}^0 + u_z n_x \Sigma_{xzx}^0 - T_x G_{xz}^0 - T_z G_{zz}^0\} d\mathbf{l}' = u_z^T(\mathbf{r}), \quad \mathbf{r} \in S_0, \quad (15)$$

$$-\frac{1}{2}u_x + \oint_{S_0} \{u_x n_x \Sigma_{xxx}^1 + u_x n_z \Sigma_{xxz}^1 + u_z n_x \Sigma_{xzx}^1 + u_z n_z \Sigma_{zzx}^1 - T_x G_{xx}^1 - T_z G_{zx}^1\} d\mathbf{l}' = 0, \quad \mathbf{r} \in S_0, \quad (16)$$

$$-\frac{1}{2}u_z + \oint_{S_0} \{u_z n_z \Sigma_{zzz}^1 + u_x n_x \Sigma_{xzz}^1 + u_x n_z \Sigma_{xxz}^1 + u_z n_x \Sigma_{xzx}^1 - T_x G_{xz}^1 - T_z G_{zz}^1\} d\mathbf{l}' = 0, \quad \mathbf{r} \in S_0. \quad (17)$$

Thus, we have four unknowns $u_x = u_x(\mathbf{r}')$, $u_z = u_z(\mathbf{r}')$, $T_x = T_x(\mathbf{r}')$, and $T_z = T_z(\mathbf{r}')$ and four scalar equations (G_{ij} and Σ_{ijk} are in fact replaced by their expressions in terms of $g_{p,s}$ before further treatment). The method of moment is then used to solve the surface unknowns. Once we know the displacement fields $\mathbf{u}(\mathbf{r}')$ and the tractions $\hat{\mathbf{n}}' \cdot \bar{\mathbf{T}}(\mathbf{r}')$ on S_0 , the original volume integrals are used to calculate the displacement fields everywhere in Ω_0 and Ω_1 . In particular in Ω_0 ($\mathbf{u} = \mathbf{u}^T + \mathbf{u}^{sc}$),

$$\mathbf{u}(\mathbf{r}) = \mathbf{u}^T(\mathbf{r}) + \int_{S_0} \{[\hat{\mathbf{n}}' \cdot \bar{\mathbf{T}}(\mathbf{r}')] \cdot \bar{\mathbf{G}}^0(\mathbf{r}, \mathbf{r}') - \mathbf{u}(\mathbf{r}') \cdot [\hat{\mathbf{n}}' \cdot \bar{\bar{\Sigma}}^0(\mathbf{r}, \mathbf{r}')]\} d\mathbf{l}', \quad \text{for } \mathbf{r} \in \Omega_0, \quad (18)$$

while the constitutive relation (3) is used to determine the stress tensor $\bar{\mathbf{T}}$. We note that for the voltage calculation, (1) is applied right on S_0 that is without need to compute the scattered fields elsewhere.

Formulation of the Linear System

To solve the surface unknowns $u_x(\mathbf{r}')$, $u_z(\mathbf{r}')$, $T_x(\mathbf{r}')$, and $T_z(\mathbf{r}')$ with the method of moment, we first discretize the surface uniformly into N subsections. Next, we expand the surface field unknowns in pulse basis functions, i.e.,

$$u_x(\mathbf{r}') = \sum_{n=1}^N u_n^x P_n(\mathbf{r}'), \quad u_z(\mathbf{r}') = \sum_{n=1}^N u_n^z P_n(\mathbf{r}'), \quad (19)$$

$$T_x(\mathbf{r}') = \sum_{n=1}^N T_n^x P_n(\mathbf{r}'), \quad T_z(\mathbf{r}') = \sum_{n=1}^N T_n^z P_n(\mathbf{r}'), \quad (20)$$

where u_n^x , u_n^z , T_n^x and T_n^z with $n = 1, \dots, N$ are the unknown coefficients to be determined. $P_n(\mathbf{r})$, $n = 1, \dots, N$ are pulse basis functions. To establish the linear algebraic equations, we

substitute these expansions in Eqs. (14-17), multiply both sides with $\delta(\mathbf{r} - \mathbf{r}_m)$, and integrate in x over the surface. As an example, the resulting first set of linear equations is written as

$$\sum_{n=1}^N (A_{mn}^1 u_n^x + B_{mn}^1 u_n^z + C_{mn}^1 T_n^x + D_{mn}^1 T_n^z) = b_m^1, \quad m = 1, 2, \dots, N, \quad (21)$$

where $A_{mn}^1, B_{mn}^1, C_{mn}^1, D_{mn}^1$ and b_m^1 are constant coefficients that are too lengthy to write down here; they depend on (n_x, n_y) , g_p and g_s (pertaining to Ω_0 and Ω_1) as well as on the latter's first (∂_i), second (∂_{ij}^2), and third-order (∂_{ijk}^3) spatial derivatives.

The matrix elements can be calculated directly from the above formulae for non-diagonal terms ($m \neq n$). For diagonal terms, the Green's functions are singular when $|\mathbf{r}' - \mathbf{r}_m|$ approaches zero. However, the integrands for both A_{mm}^1 and B_{mm}^1 are odd functions for the central point of x_m, z_m . The Cauchy principal integrals thus vanish for the self-terms yielding $A_{mm}^1 = 0.5$, $B_{mm}^1 = 0$, $m = 1, 2, \dots, N$. The diagonal elements C_{mm}^1 and D_{mm}^1 require careful evaluation. We found that the simple small argument approximation for the Hankel function which works for electromagnetic problems, causes intolerable error for the present elastic wave problem. In order to achieve good results, subdivision of the line segment into smaller ones is required [6]. The procedure briefly described above yields $4N$ linear algebraic equations with the same number of unknowns. The combined linear algebraic equations has been solved by an iterative scheme based on conjugate gradient methods.

NUMERICAL RESULTS

Validation Test: Scattering from a Flat Cement-Formation Surface

The formulation was first tested on the canonical case of a single interface separating two semi-infinite media and excited by a compressional CTP (Gaussian) beam. Here, reference solutions for the reflected and transmitted beams are obtained by spectral plane wave representations (not given here; see [7] for details) which are computed via a real-axis integration scheme. For the configuration properties given in the caption of Fig. 2, the reflected and transmitted beams shown in Fig. 2 in solid for the boundary element method (BEM) solution and in dashed for the real-axis integration (RAI) agree very well with each other and thus validate the BEM code for this configuration. The profile of the reflected (transmitted) beam in Fig. 2 departs markedly from being Gaussian because of interferences between the specularly reflected (transmitted) and the compressional head wave field which is excited by the incident beam at 20° . Extensive additional tests were conducted for various beam incidence angles and material parameters and the results showed excellent agreement between the BEM and RAI solutions.

Pulse-Echo Scattering from Sinusoidally Rough Surfaces and Effects on Voltage

As an illustration of the code use for the pulse-echo measurement addressed in this article, we compute the voltage received when S_0 is sinusoidally rough with spatial period (correlation length) Λ and amplitude h_0 (i.e., $h = h_0 \sin\{2\pi x/\Lambda\}$). It is noteworthy to plot the profile of the scattered displacement fields in the cement to gain an understanding of the effect on the voltage collected by the transducer via the steel layer. The example treated in Fig. 3 pertains to a flat surface and to a sinusoidal surface with $h_0 = 1\text{mm}$ and $\Lambda = 10, 20$ and 40mm . As can be observed in Fig. 3(a) and (c) for $|u_z|$ and $|u_x|$, the incident profile, which has an extent of approximately 80mm (this is equal to that of the scattered field from the flat surface), probes several cycles for $\Lambda = 10\text{mm}$, few cycles for $\Lambda = 20\text{mm}$, and less

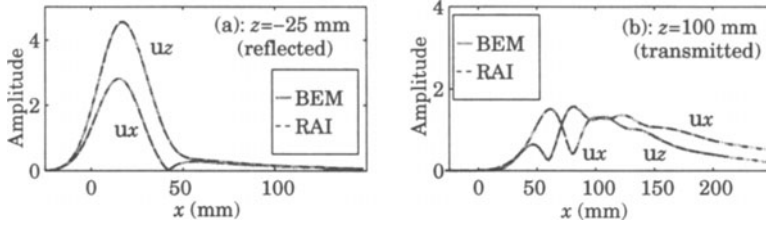


Figure 2. Amplitude of reflected (a) and transmitted (b) beams from a single flat interface between cement and formation for incidence of a Gaussian beam at 20° . Boundary element method (BEM) solution in gray solid agrees with the (reference) real-axis integration (RAI) in dashed. The compressional CTP beam input is located at $(x, z) = (0, -25)$ mm with $1/e$ width $W = 18$ mm; $f = 0.5$ MHz; Other parameters: $v_{p0} = 3000$ m/s, $v_{s0} = 2000$ m/s, $\rho_0 = 1400$ kg/m³, $v_{p1} = 6400$ m/s, $v_{s1} = 3700$ m/s, $\rho_1 = 2700$ kg/m³.

than 2 cycles for $\Lambda = 40$ mm. We then anticipate the scattering to show characteristics of a periodic structure for $\Lambda = 10$ mm whereas for $\Lambda = 40$ mm we anticipate the outcome to be dictated by geometry (i.e., specularly) with less multiple scattering taking place. The results in Fig. 3 confirm these predictions.

The amplitude of u_z and u_x are shown in Fig. 3(a) and (c) whereas their corresponding plane-wave spectra are shown in Fig. 3(b) and (d). It can be observed that the fields for the flat surface (dark solid) are smooth and fill the central region (in line with the transducer position at $x = 0$). On the other hand, the scattered fields for the rough surfaces are jagged and fill larger portion of the observation domain. The spectra are helpful in that they reveal the direction of propagation of the scattered fields. The spectrum for the flat surface is centered around the normal direction (i.e., $\theta = 0^\circ$) for both displacement components. On the other hand, the spectra for the scattered fields from the rough surfaces show energy distribution over a larger angular range (but within $\pm 40^\circ$). We observe, in particular, the discrete spectral distribution of the fields for $\Lambda = 10$ mm reminiscent of the Floquet-type scattering as noted above. For this case ($\lambda = 10$ mm), the peaks of spectra in Fig. 3(b) and (d) occur very close to $\sin^{-1}\{2\pi/\Lambda/k_f\} = \pm 17.5^\circ$ and twice this amount thus confirming our conclusion. The field spectra for $\Lambda = 20$ mm exhibits a peak around $\pm 8.7^\circ$ which lines up with $\sin^{-1}\{2\pi/\Lambda/k_f\}$ as well. However, the spectra curves for $\Lambda = 40$ mm exhibit mostly a specular deviation from the $\theta = 0^\circ$ direction. Note that the field amplitude and spectral profiles pertaining to the rough surfaces are not symmetric with respect to the central position ($x = 0$ or $\theta_f = 0$) because the rough surfaces are not symmetric with respect to $x = 0$.

On the basis of the plane-wave spectra of the scattered fields, we can anticipate qualitatively the outcome for the voltage collection process. The voltage is strong for energy scattered in the central angular region and becomes weak when energy is deviated away from the central region thus either missing the collecting aperture (via the steel) or impinging incoherently enough to average out to a small quantity. These observations are confirmed by the voltage magnitude computed using (1) and plotted in Fig. 4, for sinusoidal roughness with various h_0 and Λ . The data point at $\Lambda = 0$ refers to a flat surface S_0 . It can be observed that there is a pronounced voltage drop when the incident field interacts strongly with the roughness. For the incident field with compressional wavelength

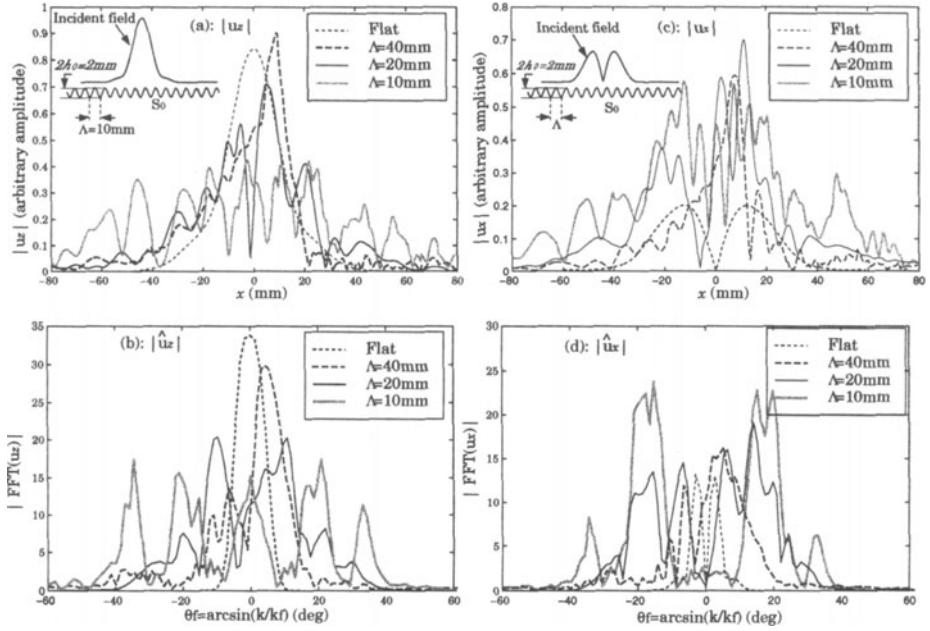


Figure 3. Amplitude of scattered u_z (a) and u_x (c) displacement fields due to sinusoidally rough surface S_0 and their corresponding plane wave spectra in (b) and (d) for three different spatial periods Λ and for an amplitude $h_0 = 1\text{mm}$. For reference, the curves for a flat surface are also included. Fields computed in the cement ($z = -20\text{mm}$) with BEM code for pulse-echo configuration as shown in Fig. 1(b). The pulse-echo CTP transducer is located at $(x, s) = (0, 25.4)\text{mm}$ with $1/e$ width $W = 12\text{mm}$; $f = 0.5\text{ MHz}$; Other parameters: $v_{\text{fluid}} = 1480$, $\rho_{\text{fluid}} = 1000\text{kg/m}^3$; $v_{\text{p,steel}} = 5880\text{m/s}$, $v_{\text{p,steel}} = 3220\text{m/s}$, $\rho_{\text{steel}} = 7800\text{kg/m}^3$, $h_1 = 9.5\text{mm}$; $v_{p0} = 3500\text{m/s}$, $v_{s0} = 2400\text{m/s}$, $\rho_0 = 1650\text{kg/m}^3$, $v_{p1} = 6000\text{m/s}$, $v_{s1} = 3500\text{m/s}$, $\rho_1 = 2700\text{kg/m}^3$, $h_2 = 25.4\text{mm}$. Compressional wavelength in cement is $\lambda_{p0} = 7\text{mm}$.

$\lambda_{p0} = 7\text{mm}$, this occurs for a reasonable roughness amplitude ($h_0 > 1\text{mm}$) and when Λ is of the order of λ_{p0} . For large Λ 's ($> 20\text{mm}$), specularity dictates the outcome and the voltage then depends on the amplitude of roughness as well as the surface position with respect to the transducer. In this sense, the data points pertaining to $\Lambda = 40\text{mm}$ and $h_0 = 1, 2$ and 4mm in Fig. 4 are expected to change with a lateral translation of S_0 .

CONCLUSIONS

In this article, we have briefly described the development of a 2D single-frequency hybrid analytical/numerical model for ultrasonic pulse-echo measurements as applied to cased well evaluations. The model emphasizes the effects on the transducer voltage due to roughness at the cement-formation interface. The analytical part consists of the complex-transducer-point technique and plane-wave decomposition and synthesis which are utilized to formulate the transmitted fields in the cement layer. Whereas, the numerical part consists of a surface integral equation to formulate the scattered field from the rough surface. The transducer voltage due to scattering from the rough surface is expressed as an integral over that surface. The model is numerically implemented via a real-axis integration (RAI) scheme to compute the spectral integrals for the transmitted fields and via a boundary element method (BEM) to solve for the surface integral equation.

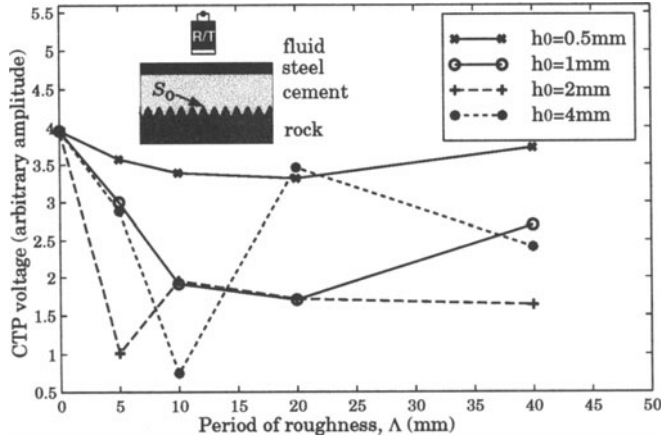


Figure 4. Amplitude of CTP voltage due to scattering from flat S_0 (data point for $\Lambda = 0$) and sinusoidally rough S_0 with various periods Λ and amplitude h_0 . A pronounced drop in voltage occurs for resonable roughness height ($h_0 > 1\text{mm}$) and roughness period Λ close to the compressional wavelength of the incident field (i.e., $\lambda_{p0} = 7\text{mm}$). Parameters as in Fig. 3.

We have included illustrative numerical results for a single solid-solid surface where the BEM code is validated against a reference RAI code and for the pulse-echo measurement with sinusoidally rough cement-formation surfaces. The numerical code is presently being used to study real roughness effects as well as provide reference data to assess approximate but more computationally-efficient numerical schemes to treat scattering from roughness.

ACKNOWLEDGMENT

This work was conducted while Y-H Chen was on leave from the Center for Computational Electromagnetics, Department of Electrical and Computer Engineering, University of Illinois, IL 61801.

REFERENCES

1. A. J. Hayman, R. Hutin, and P. V. Wright, "High-resolution cementation and corrosion imaging by ultrasound," In SPWLA 32nd Annual Symposium, June 16-19, 1991, TX.
2. C. J. Randall and F. E. Stanke, "Mathematical model for internal inspection of cylindrically layered structures," J. Acoust. Soc. Am. **83**, 1295-1305 (1988).
3. S. Zeroug, F. E. Stanke, and R. Burridge, "A complex-transducer-point model for emitting and receiving ultrasonic transducers", Wave Motion **24**, 21-40 (1996).
4. A. T. de Hoop, "Reciprocity theorems for acoustic wave fields in fluid/solid configurations," J. Acoust. Soc. Am. **87** 1932-1937 (1990).
5. Pao, Yih-Hsing and Varatharajulu, V., "Huygens' principle, radiation conditions, and integral formulas for the scattering of elastic waves," J. Acoust. Soc. Am., **59**, 1361-1371 (1976).
6. Manuscript in preparation.
7. Y. H. Chen, W. C. Chew, and S. Zeroug, "Fast multipole method as an efficient solver for 2D elastic wave surface integral equations," Accepted for publication in Journal of Computational Mechanics (1997).